

Research Article

Experimental Investigation and Load Capacity of Slender Cold-Formed Lipped Channel Sections with Holes in Compression

Xingyou Yao ^{1,2}

¹Jiangxi Province Key Laboratory of Hydraulic and Civil Engineering Infrastructure Security, Nanchang Institute of Technology, Nanchang 330099, China

²School of Civil Engineering and Architecture, Nanchang Institute of Technology, Nanchang 330099, China

Correspondence should be addressed to Xingyou Yao; yaoxingyoujd@163.com

Received 21 December 2020; Revised 8 June 2021; Accepted 1 July 2021; Published 12 July 2021

Academic Editor: Stefano de Miranda

Copyright © 2021 Xingyou Yao. This is an open access article distributed under the Creative Commons Attribution License, which permits unrestricted use, distribution, and reproduction in any medium, provided the original work is properly cited.

The use of cold-formed steel (CFS) channels with circular or rectangular web holes is becoming increasingly popular in building structures. However, such holes can result in sections becoming more susceptible to buckle and display lower load-carrying capacities. This paper presents a total of 42 axial compression tests of CFS lipped channel slender columns with and without circular and rectangular web holes, including different hole sizes and cross sections. The test results show that the axial members with a small ratio of width to thickness were governed by global buckling, while the members with a large ratio of width to thickness were controlled by the interaction of local, distortional, and global buckling. The axial strength decreased maximum by 20.48% and 22.98% for the member with circular holes and rectangular holes, compared to a member without a web hole. Then, a nonlinear elastoplastic finite element model (FEM) was developed, and the analysis results showed good agreement with the test results. The validated FE model was used to conduct a parametric study involving 36 FEMs to investigate the effects of column slenderness, dimension of the hole, and the number of holes on the axial strength of such channels. Furthermore, the formulas to predict the global buckling coefficient and the effective area were modified for such sections with holes by using the verified FEM. Finally, the tests and parametric study results were compared against the design strengths calculated in accordance with the developed method. The comparison results show that the proposed design method closely predicts the axial capacity of CFS channels with circular or rectangular web holes.

1. Introduction

The CFS lipped channel sections have been widely used in buildings as walls, floors, and ceilings due to their high-strength-to-weight ratio and ease of construction. However, the holes often appear in the web because of the installation of electrical, plumbing, and heating conduits for such lipped channel sections. The occurrence of holes in the web would decrease the cross-section area and stiffness.

In the literature, some work has been reported on the buckling behavior and the reduction in compression resistance of channel sections having web openings. Stub column tests conducted by Colberg [1] indicated that the load-carrying capacity decreased with the increasing of the ratio of circular hole diameter-to-depth of the web. The same

conclusions have also been reported for stub columns with circular, rectangular, and slotted web holes [2, 3]. The compression tests of 24 short and intermediate CFS lipped channel columns with and without slotted web holes showed that the presence of slotted holes caused a slight decrease in the ultimate capacity [4]. The axially compressed tests of intermediate length CFS lipped channel columns with circular holes indicated that the stress of the plate adjacent to the circular hole was higher than that of other parts and the plate adjacent to the circle hole yielded early [5]. For lipped channel columns with web stiffener, numerical and experimental studies were carried out to analyze the effects of holes on the failure mode and load-carrying capacity by Yao et al. [5]. The results demonstrated that the holes led to the change of buckling mode and decreased the ultimate

strength. The modified direct strength method was developed based on the test results by Moen and Schafer [6, 7]. The effects of holes on the buckling behavior of CFS channels under axial compression were studied by Kulatunga et al. [8, 9], and it was found that the ultimate failure load of the channels under compression varied greatly with the presence of holes.

In the literature, some other significant work has been reported on the reduction in strength of channel sections having openings covering shear by Pham [10], Pham et al. [11], and Keerthan and Mahendran [12, 13], and the bending of the beam by Moen et al. [14] and Zhao et al. [15, 16].

Recently, Chen et al. [17–19] reported experimental and numerical studies on the axial strength of single channels and back-to-back channels with edge-stiffened holes and found that the axial strength of channels with edge-stiffened holes was greater than those of plain channels. Meanwhile, some other work has been reported on the strength of channel sections having edge-stiffened holes covering web crippling by Uzzaman et al. [20, 21].

In the literature, limited work has been reported on CFS slender channels with holes in the web. A total of 21 channel specimens test, including C-shaped cross sections with and without web openings conducted by Dung et al. [22]. The flexural-torsional buckling was observed for all slender compressive specimens and the average strength of the specimen was slightly reduced because of the web opening. In order to develop the effective width method to predict the load capacity of a channel with holes, an approximate method to predict the elastic buckling stress of plates with holes was developed [23]. Meanwhile, the simplified methods to predict the local, distortional, and global critical elastic buckling loads of CFS columns with holes were developed based on theoretical and FE analysis for developing the direct strength method to calculate the strength of CFS columns with holes [24–26].

In terms of the design standards, the American Iron and Steel Institute (AISI) [27] and the Australian and New Zealand Standards (AS/NZS) [28] do not provide sufficient effective width design rules for determining the axial capacity of CFS channels with holes because the reduced effective width design method is only suitable to members with relatively small holes in these codes. The direct strength method is given in AISI for determining the axial capacity of CFS channels with holes, but the elastic buckling capacity of members with holes needs to be calculated by using the finite element method or complicated formula. Meanwhile, there is no design provision about the perforated plates and members in the Chinese code [29].

As mentioned previously in the literature, most of the researches considered the buckling behavior and design method of the stud and intermediate length CFS channels with small holes. Nevertheless, limited work has been reported on slender columns with large holes under axial compression. Thus, this paper reports 42 new experiments on the axial strength of CFS slender lipped channels with circular and rectangular holes in the web. Tensile coupon tests were also conducted to determine the material properties of the channels. A nonlinear elastoplastic FE model

was then developed and validated against the test results in terms of ultimate strength and buckling modes. Using the validated FE model, a parametric study involving 36 models was conducted to investigate the effects of column slenderness, hole size, and the number of holes on the axial strength of such columns. The proven FEM was used to develop the global buckling coefficient equation and effective area formula of the CFS lipped channel section under axial compression, considering the effect of holes. Finally, the prediction method of ultimate axial strength of CFS lipped channels with holes in the web was proposed and the design strengths were compared against both the test and FEA results.

2. Experimental Investigation

2.1. Test Specimens. This test employed 42 CFS lipped channel axially compressed members. There were 6 non-perforated members, 18 members with circular holes, and 18 members with rectangular holes. The definitions of geometric parameters of the specimen and the location, spacing, and types of holes are illustrated in Figure 1. Four cross sections $75 \times 40 \times 10 \times 0.8$ mm, $75 \times 40 \times 10 \times 1$ mm, $90 \times 50 \times 15 \times 0.8$ mm, and $80 \times 60 \times 10 \times 0.8$ mm ($h \times b \times a \times t$, h : web depth, b : flange width, a : lip length, t : thickness) were selected. The nominal thicknesses of the specimens are 0.8 mm and 1.0 mm. The diameters of circular holes are 0.3, 0.5, and 0.7 to the web depth. The heights of the rectangular holes are 0.2, 0.4, and 0.6 to the web depth. The ratio of length-to-width (L_h/H_h) of the rectangular hole is equal to 2. Each specimen is 2000 mm and has three holes. The hole spacings are 500 mm and 600 mm for members with circular and rectangular holes, respectively. The labeling rule of all specimens is defined in Figure 2. The nominal and measured dimensions of all specimens are tabulated in Table 1.

2.2. Material Properties. Steel sheets of grade LQ550 with two kinds of thicknesses were selected to manufacture the specimens. 3 tensile coupon tests of steel sheets with different thicknesses were conducted to determine the material properties based on Chinese specifications of “Tensile tests of metallic materials part 1: test methods at room temperature” (GB/T228.1-2010) [30]. The stress-strain curves of one of the coupons for every kind of steel plate are shown in Figure 3, and the other stress-strain curves are the same as these curves. The measured average material properties, including the static 0.2% proof stress ($f_{0.2}$), initial Young’s modulus (E), ultimate strength (f_u), and ultimate strain (ϵ_u), are listed in Table 2.

2.3. Initial Geometric Imperfections. Initial geometric imperfections are usually generated in cold form and transportation, which has a great effect on the buckling behavior of CFS members. Initial geometric imperfections along the longitudinal direction of all specimens were measured before tests. The initial geometric imperfections were measured with an interval of 150 mm along the specimen length. The

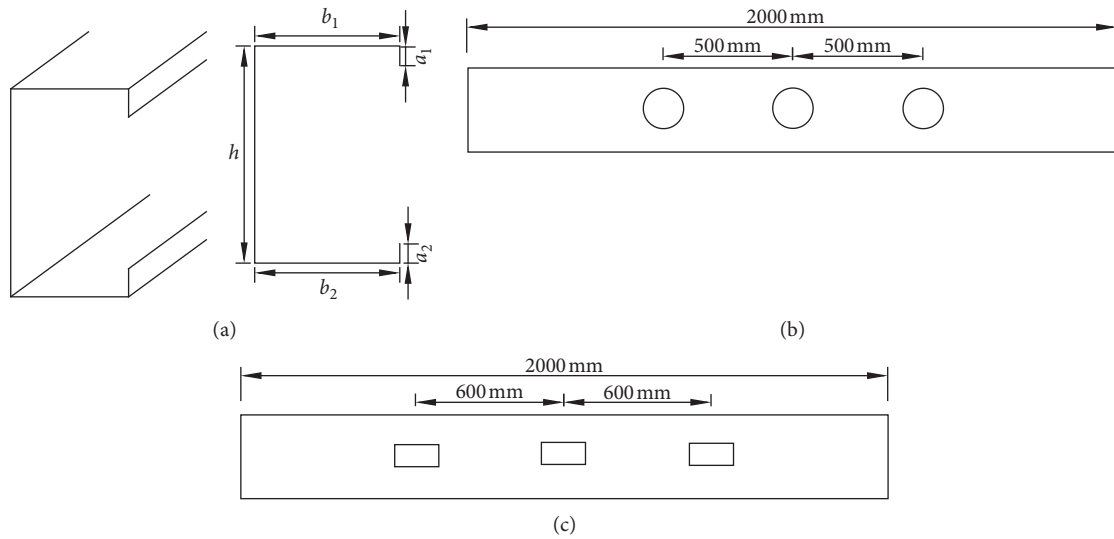


FIGURE 1: Section dimensions and hole size of CFS lipped channel columns: (a) lipped channel section, (b) web with circular holes, and (c) web with rectangular holes.

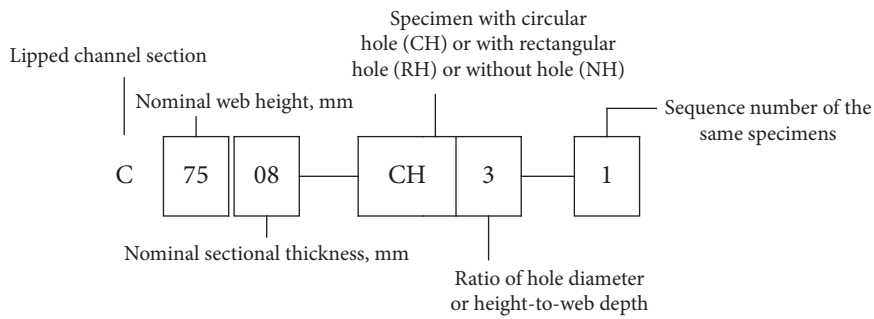


FIGURE 2: Specimen labeling.

TABLE 1: Nominal and measured section dimensions of specimens.

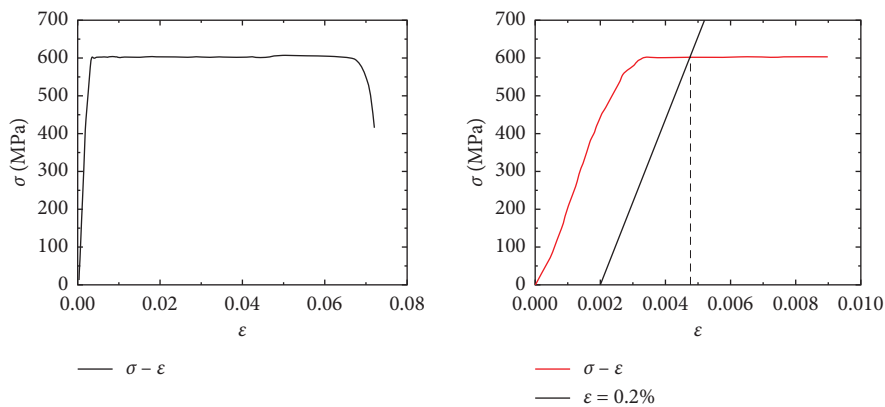
Specimen	Nominal section dimensions					Measured section dimensions					Maximum of initial geometric imperfections Δ_{max} (mm)	
	h (mm)	b (mm)	a (mm)	t (mm)	Slenderness ratio	L (mm)	h_1 (mm)	b_1 (mm)	b_2 (mm)	a_1 (mm)		a_2 (mm)
C7508-CH3-1						2000.00	74.73	38.51	40.35	9.75	8.87	0.927
C7508-CH3-2						2000.00	73.94	39.81	39.34	9.65	9.72	1.062
C7508-CH5-1	75	40	10	0.8	89.91	1999.95	74.66	38.95	38.93	10.31	9.69	0.823
C7508-CH5-2						2000.00	73.78	39.63	39.73	9.57	10.06	1.326
C7508-CH7-1						1999.60	74.01	39.58	39.58	9.56	9.84	1.856
C7508-CH7-2						1999.70	73.92	38.95	39.83	10.22	9.64	0.902

TABLE 1: Continued.

Specimen	Nominal section dimensions					Measured section dimensions					Maximum of initial geometric imperfections	
	h (mm)	b (mm)	a (mm)	t (mm)	Slenderness ratio	L (mm)	h_1 (mm)	b_1 (mm)	b_2 (mm)	a_1 (mm)	a_2 (mm)	Δ_{\max} (mm)
C7510-NH-1						2000.00	75.05	39.97	39.84	9.98	9.84	0.812
C7510-NH-2						2000.10	75.13	39.95	40.00	9.85	9.98	1.856
C7510-RH2-1						2001.25	74.51	39.50	39.69	9.39	9.92	0.925
C7510-RH2-2	75	40	10	1	90.55	2001.15	73.97	39.24	38.91	10.00	10.50	0.756
C7510-RH4-1						2001.20	73.70	40.09	39.47	9.52	9.93	1.012
C7510-RH4-2						2001.10	74.04	39.45	39.41	9.70	10.04	1.201
C7510-RH6-1						2001.25	73.91	39.35	39.68	9.83	9.86	0.856
C7510-RH6-2						2001.15	74.10	38.83	39.83	9.90	9.44	0.914
C9008-NH-1						2000.05	89.96	49.69	49.67	14.83	14.95	1.302
C9008-NH-2						1999.85	89.91	50.02	50.04	14.86	14.84	1.202
C9008-CH3-1						1999.25	89.82	48.95	50.13	14.21	14.45	0.852
C9008-CH3-2						1999.25	89.85	48.18	49.27	15.48	14.58	0.962
C9008-CH5-1						1999.55	88.25	49.65	50.81	14.09	14.71	0.861
C9008-CH5-2						1999.50	89.97	50.26	49.52	14.02	14.53	0.934
C9008-CH7-1	90	50	15	0.8	72.38	1999.58	89.99	50.26	49.52	14.02	14.53	1.023
C9008-CH7-2						1999.62	89.97	50.26	49.52	14.02	14.53	0.954
C9008-RH2-1						1999.60	89.96	49.79	49.60	13.96	14.84	0.895
C9008-RH2-2						1999.70	89.26	49.65	49.93	14.29	15.33	0.697
C9008-RH4-1						1999.95	89.07	48.45	49.08	15.57	14.52	1.203
C9008-RH4-2						2000.05	89.58	49.76	48.86	14.60	14.70	1.322
C9008-RH6-1						1999.80	90.01	49.35	49.29	14.71	14.77	0.891
C9008-RH6-2						1999.85	89.95	49.57	49.38	15.04	14.78	1.849

TABLE 1: Continued.

Specimen	Nominal section dimensions					Measured section dimensions					Maximum of initial geometric imperfections	
	h (mm)	b (mm)	a (mm)	t (mm)	Slenderness ratio	L (mm)	h_1 (mm)	b_1 (mm)	b_2 (mm)	a_1 (mm)	a_2 (mm)	Δ_{max} (mm)
C8008-NH-1						2000.05	80.02	59	59.04	9.84	9.86	2.467
C8008-NH-2						1999.8	79.89	60.03	60.07	9.6	9.58	1.312
C8008-CH3-1						1999.7	79.88	59.62	60.27	8.88	9.11	1.512
C8008-CH3-2						1999.85	79.14	60.58	59.84	9.62	8.49	0.912
C8008-CH5-1						2000.05	80.22	59.10	59.41	10.01	9.32	1.325
C8008-CH5-2						1999.9	79.66	59.34	59.46	9.87	9.40	0.816
C8008-CH7-1	80	60	10	0.8	82.00	2000	79.90	58.71	59.28	9.75	9.81	0.988
C8008-CH7-2						2000.05	80.43	58.70	59.01	10.07	9.70	1.324
C8008-RH2-1						2000.10	79.29	59.33	59.40	9.74	9.92	1.624
C8008-RH2-2						2000.15	79.48	59.02	59.86	10.22	9.16	1.214
C8008-RH4-1						1999.95	80.24	59.80	58.75	9.61	9.22	1.212
C8008-RH4-2						2000.00	80.51	58.67	59.10	10.02	9.39	0.897
C8008-RH6-1						1999.90	78.25	59.10	59.02	10.92	9.80	1.245
C8008-RH6-1						2000.00	79.80	59.48	59.26	9.09	9.30	1.311



(a)

FIGURE 3: Continued.

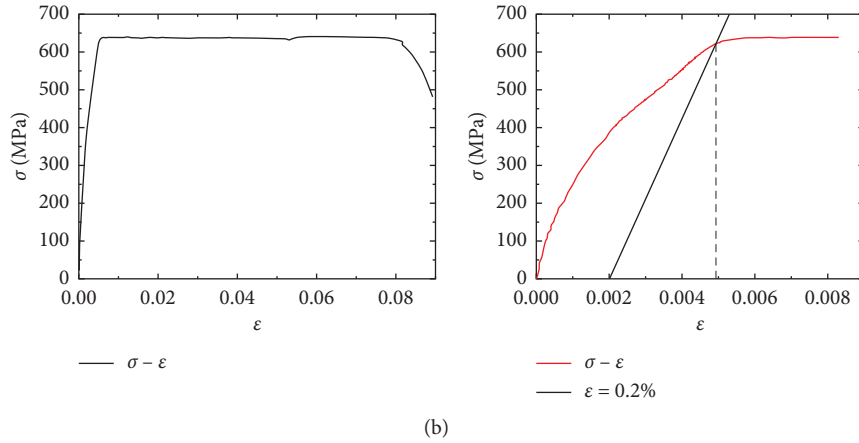


FIGURE 3: Stress-strain curves of coupon test. (a) Thickness $t = 0.80$ mm. (b) Thickness $t = 1.00$ mm.

TABLE 2: Mean value of coupon tests.

t (mm)	$f_{0.2}$ (MPa)	f_u (MPa)	E (MPa)	ϵ_u (%)
0.80	600	602	2.16×10^5	7.19
1.00	620	634	2.15×10^5	8.92

measuring locations at cross section are illustrated in Figure 4(a), which was suggested in reference [31]. The locations 1, 2, 3, and 4 indicate the deviations from flats for the initial local geometric imperfection, the initial distortional geometric imperfection, the initial global geometric imperfection about the weak axis, and the initial global geometric imperfections about the great axis, respectively. The dial gauge was used to measure the initial geometric imperfection, as shown in Figure 4(b). Table 1 lists the maximum magnitudes (Δ_{\max}) of four kinds of initial geometric imperfections for all specimens. The initial geometric imperfections along the longitudinal direction for specimens C7510-NH-1, C7508-CH3-1, C8008-NH-1, and C9008-NH-1 are illustrated in Figures 5(a)–5(d), respectively. The initial geometric imperfections of the other specimens have almost the same distribution as these specimens. The measured initial geometric imperfections indicate that the imperfections have no obvious rules along the longitudinal direction, but the initial distortional geometric imperfection magnitudes are more than the initial local geometric imperfections and initial global geometric imperfections, and the specimens with large width-to-thickness ratio have bigger initial geometric imperfection magnitudes.

2.4. Test Rig and Procedure. The specimens were loaded by a 50 kN Hydraulic Jack and reaction frame system as shown in Figure 6. The upper actuator and lower pedestal were fitted with 250 mm \times 200 mm \times 8 mm steel platen ground flat and parallel. The column specimens were put directly on the steel platen as they were compressed. Friction between the column ends and the steel platens were the only lateral forces that restrained the column cross section under load. The axial compressive loading was obtained from the load cell positioned at the top of the test specimens. To understand

clearly the displacement, deformation, and stress of the specimen during the loading process, the position transducers and strain gauges were set up as suggested in reference [31]. For specimens without holes, four-position transducers (Figure 7(a)) and four strain gauges (Figure 7(b)) were arranged at the mid-height of the column and a position transducer is arranged at the upper end plate of the specimen to measure the vertical displacement under load. For specimens with holes, four strain gauges (Figure 7(c)) were adhered at the middle height location and four strain gauges (Figure 7(d)) were adhered at the locations which are higher 100 mm than mid-height. Four-position transducers (Figure 7(e)) were arranged at the middle location to measure the displacement of web adjacent to the hole and flanges. Three-position transducers (Figure 7(f)) were set up at the web, which is higher 100 mm than the mid-height of specimens. All the test data could be obtained by using the YJ16 data acquisition instrument.

3. Test Results

3.1. Failure Buckling Mode and Load-Strain Curve. Table 3 presents the results of 42 axially compressed specimens about buckling modes and load capacities in this experiment, where L , D , FT , and F represent the local buckling, distortional buckling, flexural-torsional buckling, and flexural buckling, respectively; P_b , P_a , P_c are the test result, finite element analysis result, and calculated result by using the proposed method, respectively.

As shown in Table 3, all specimens with circular holes exhibited an obvious interaction of local buckling (see Figure 8(a)), distortional buckling (see Figure 8(b)), and global buckling (see Figure 8(c)) (flexural buckling or flexural-torsional buckling). For global buckling, section C7508 with small width to thickness exhibited flexural-torsional buckling,

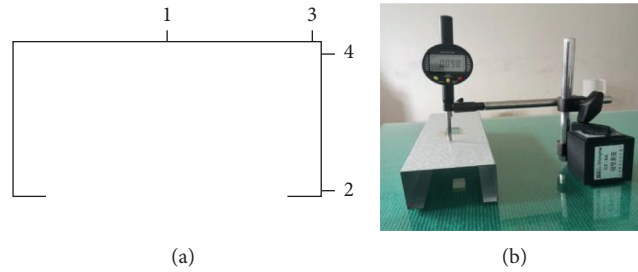


FIGURE 4: Measure of the longitudinal initial geometric imperfection at cross section. (a) Measured location. (b) Measured setup.

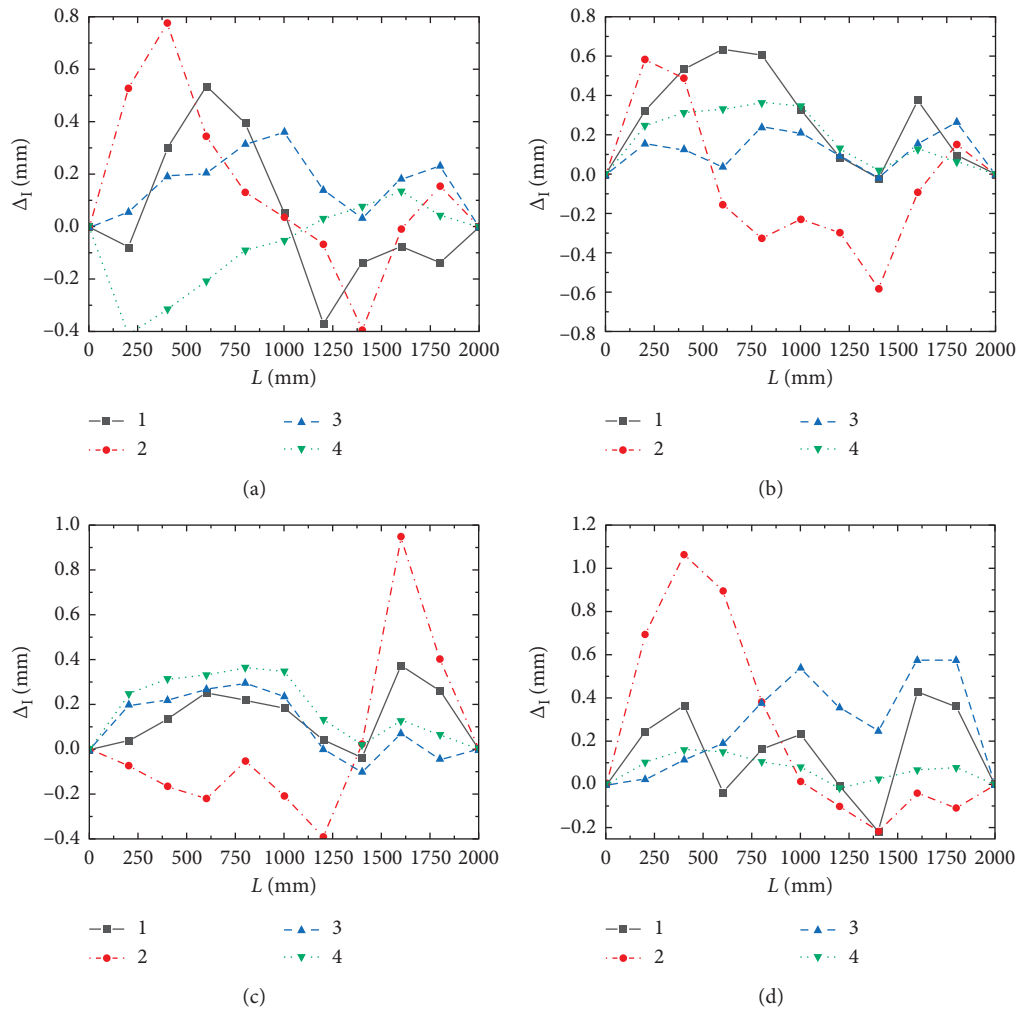


FIGURE 5: Initial geometric imperfections of specimens. (a) C7510-NH-1. (b) C7508-CH3-1. (c) C8008-NH-1. (d) C9008-NH-1.

section C8008 and section C9008 with the size of holes $d/h=0.3$ and 0.5 displaying flexural-torsional buckling, and section C8008 and section C9008 with the size of holes $d/h=0.7$ displaying flexural buckling. The interaction buckling progression under load for specimen C8008-CH7-1 is depicted in Figure 8.

The test buckling mode in Table 3 indicates that all specimens with rectangular holes for section C8008 and C9008 with large width-to-thickness ratio exhibited obvious interaction of local buckling, distortional buckling, and

global buckling. The section with small holes exhibited flexural-torsional buckling and flexural buckling occurred for the section with large holes. Section C7510 displayed the flexural-torsional buckling because of the small width-to-thickness ratio. Specimen C7510-RH6-1 is depicted in Figure 9 as an example. The buckling deformations for all other specimens with circular and rectangular holes are provided in reference [32].

The influence of the circular and rectangular holes on the buckling load of columns and the stress of the web adjacent

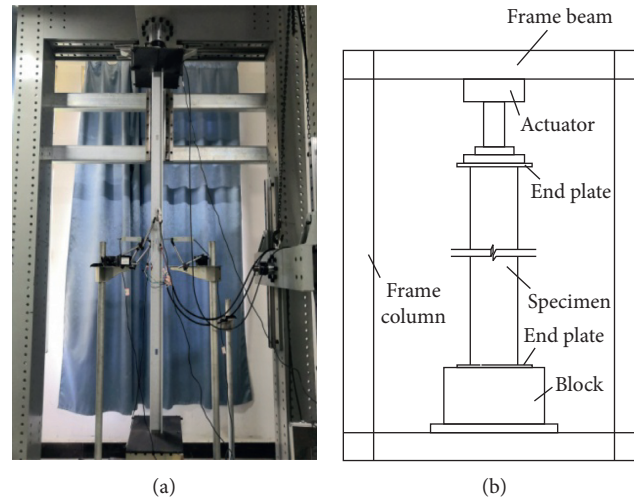


FIGURE 6: Test setup.

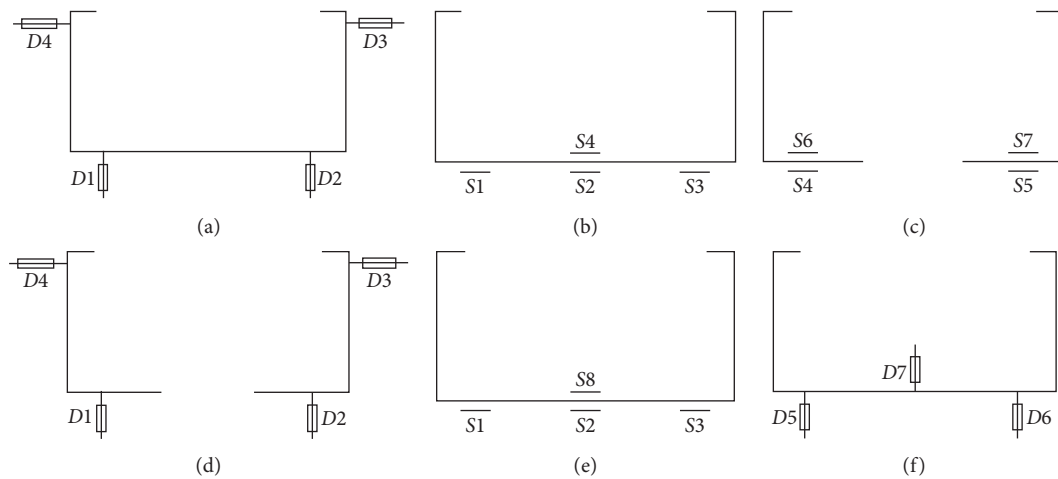


FIGURE 7: Position transducers and strain gauge arrangement. (a) Position transducers at midheight for a nonperforated specimen. (b) Strain gauges at midheight for a nonperforated specimen. (c) Strain gauges at midheight for a perforated specimen. (d) Position transducers at midheight for a perforated specimen. (e) Strain gauges at higher 100 mm than midheight for a perforated specimen. (f) Position transducers at higher 100 mm than midheight for a perforated specimen.

to the hole are provided in Figures 10 and 11 for section C9008, respectively. The results of Figures 10 and 11 indicate that the buckling stress of the web adjacent to the hole and buckling loads of specimens significantly increased with the increasing of the size of holes and the circular and rectangular holes have a significant impact on the stress concentration and distribution of CFS lipped channel columns.

Figures 12 and 13 depict the web stress response of section C9008 with circular and rectangular holes at the edge of the hole (strain gauge 4) and the same transverse location but higher 100 mm than mid-height (strain gauge 1), respectively. The comparisons show that the web stress at the edge of the hole is higher than that of the other longitudinal locations because of the stress concentrate led by the hole. Meanwhile, the stress increases obviously with the increase of the size of holes.

3.2. Load Capacities and Load-Displacement Curve. Experimental ultimate capacities for all specimens with circular holes and rectangular holes are summarized in Table 3. The load capacities reduce with a decreased value of 6.7% and 13.13% when the ratio of hole diameter-to-web depth increases from 0.3 to 0.5 and 0.7 for section C7508, respectively. The reduction values of load capacity are 7.42%, 15%, 20.48%, and 6.72%, 11.99%, and 18.28% when the ratio of hole diameter-to-web depth increases from 0 to 0.3, 0.5, 0.7 for sections C9008 and C8008, respectively. The load capacities reduce with a reduction value of 12.56%, 17.27%, and 22.98%, 3.4%, 7.38%, and 19.78%, and 4.88%, 7.25%, and 17.02% when the ratio of hole height-to-web depth increases from 0 to 0.2, 0.4, and 0.6 for sections C7510, C9008, and C8008, respectively. The comparison results indicate that the ultimate capacities of the specimens decreased obviously with the increase of the size of circular and rectangular holes.

TABLE 3: Comparison of buckling modes and ultimate capacities obtained from test, FEA, and predictions by using the proposed method.

Specimen	Test buckling mode	FEA buckling mode	P_t (kN)	Decrease of load capacities (%)	P_a (kN)	P_c (kN)	P_t/P_a	P_t/P_c
C7508-CH3-1	<i>L+D+FT</i>	<i>L+D+FT</i>	16.39		16.82	15.48	0.97	1.06
C7508-CH3-2	<i>L+D+FT</i>	<i>L+D+FT</i>	16.58		16.75	15.94	0.99	1.04
C7508-CH5-1	<i>L+D+FT</i>	<i>L+D+FT</i>	15.38	6.70	16.47	15.15	0.93	1.02
C7508-CH5-2	<i>L+D+FT</i>	<i>L+D+FT</i>	15.38	6.70	16.14	14.97	0.95	1.03
C7508-CH7-1	<i>L+D+FT</i>	<i>L+D+FT</i>	14.60	11.43	15.29	13.49	0.96	1.08
C7508-CH7-2	<i>L+D+FT</i>	<i>L+D+FT</i>	14.32	13.13	15.53	13.53	0.92	1.06
C7510-NH-1	<i>FT</i>	<i>FT</i>	27.78		28.06	25.61	0.99	1.08
C7510-NH-2	<i>FT</i>	<i>FT</i>	26.93		27.61	25.32	0.98	1.06
C7510-RH2-1	<i>FT</i>	<i>FT</i>	23.92	12.56	25.03	23.57	0.96	1.01
C7510-RH2-2	<i>FT</i>	<i>FT</i>	24.37	10.91	26.32	24.16	0.93	1.01
C7510-RH4-1	<i>FT</i>	<i>FT</i>	23.96	12.41	24.56	23.22	0.98	1.03
C7510-RH4-2	<i>FT</i>	<i>FT</i>	22.63	17.27	24.90	23.22	0.91	0.97
C7510-RH6-1	<i>FT</i>	<i>FT</i>	21.45	21.59	22.08	21.08	0.97	1.02
C7510-RH6-2	<i>FT</i>	<i>FT</i>	21.07	22.98	22.17	20.98	0.95	1.00
C9008-NH-1	<i>L+D+FT</i>	<i>L+D+FT</i>	23.72		23.94	23.31	0.99	1.02
C9008-NH-2	<i>L+D+FT</i>	<i>L+D+FT</i>	24.52		23.92	23.52	1.02	1.04
C9008-CH3-1	<i>L+D+FT</i>	<i>L+D+FT</i>	22.33	7.42	21.60	22.06	1.03	1.01
C9008-CH3-2	<i>L+D+FT</i>	<i>L+D+FT</i>	22.67	6.01	22.09	22.49	1.03	1.01
C9008-CH5-1	<i>L+D+FT</i>	<i>L+D+FT</i>	21.46	11.03	21.02	21.38	1.02	1.00
C9008-CH5-2	<i>L+D+FT</i>	<i>L+D+FT</i>	20.50	15.00	21.28	21.45	0.96	0.96
C9008-CH7-1	<i>L+D+F</i>	<i>L+D+F</i>	19.18	20.48	19.58	19.09	0.98	1.00
C9008-CH7-2	<i>L+D+F</i>	<i>L+D+F</i>	19.41	19.53	20.03	19.06	0.97	1.02
C9008-RH2-1	<i>L+D+FT</i>	<i>L+D+FT</i>	23.30	3.40	24.62	22.06	0.95	1.06
C9008-RH2-2	<i>L+D+FT</i>	<i>L+D+FT</i>	24.80	x2.82	25.37	22.52	0.98	1.10
C9008-RH4-1	<i>L+D+FT</i>	<i>L+D+FT</i>	22.88	5.14	22.87	22.72	1.00	1.01
C9008-RH4-2	<i>L+D+FT</i>	<i>L+D+FT</i>	22.34	7.38	21.97	22.72	1.02	0.98
C9008-RH6-1	<i>L+D+F</i>	<i>L+D+F</i>	19.35	19.78	19.49	20.48	0.99	0.94
C9008-RH6-2	<i>L+D+F</i>	<i>L+D+F</i>	19.50	19.15	20.89	20.57	0.93	0.95
C8008-NH-1	<i>L+D+FT</i>	<i>L+D+FT</i>	20.37		19.73	20.83	1.03	0.98
C8008-NH-2	<i>L+D+FT</i>	<i>L+D+FT</i>	20.99		20.63	20.53	1.02	1.02
C8008-CH3-1	<i>L+D+FT</i>	<i>L+D+FT</i>	19.30	6.67	18.59	19.24	1.04	1.00
C8008-CH3-2	<i>L+D+FT</i>	<i>L+D+FT</i>	19.45	5.95	18.37	19.69	1.06	0.99
C8008-CH5-1	<i>L+D+FT</i>	<i>L+D+F</i>	18.38	11.12	17.33	19.16	1.06	0.96
C8008-CH5-2	<i>L+D+FT</i>	<i>L+D+FT</i>	18.20	11.99	17.51	19.19	1.04	0.95
C8008-CH7-1	<i>L+D+F</i>	<i>L+D+F</i>	17.27	16.49	17.03	17.50	1.01	0.99
C8008-CH7-2	<i>L+D+F</i>	<i>L+D+F</i>	16.90	18.28	17.21	17.51	0.98	0.97
C8008-RH2-1	<i>L+D+FT</i>	<i>L+D+FT</i>	20.60	0.39	19.91	19.68	1.03	1.05
C8008-RH2-2	<i>L+D+FT</i>	<i>L+D+FT</i>	19.67	4.88	19.76	20.00	1.00	0.98
C8008-RH4-1	<i>L+D+F</i>	<i>L+D+F</i>	19.18	7.25	19.28	19.80	0.99	0.97
C8008-RH4-2	<i>L+D+F</i>	<i>L+D+F</i>	19.40	6.19	18.77	19.90	1.03	0.97
C8008-RH6-1	<i>L+D+F</i>	<i>L+D+F</i>	18.34	11.32	18.19	18.66	1.01	0.98
C8008-RH6-1	<i>L+D+F</i>	<i>L+D+F</i>	17.16	17.02	17.74	18.10	0.97	0.95
Average							0.989	1.008
Standard deviation							0.038	0.040
Coefficient of variation							0.039	0.040

Figures 14 and 15 depict the comparison of load-displacement curves of section C9008 with various sizes of circular and rectangular holes, respectively. It can be observed that the load capacity decreases with the increase of the size of holes.

4. Verification of Finite Element Models

The finite element program ABAQUS [33] was used to simulate the buckling modes and behavior of the specimens and perform further parametric analysis on the CFS lipped channel axially compressed columns with circular and rectangular holes. The S4R shell element was selected for the

modeling column and the analytical rigid body element was used for modeling the upper and lower end steel plates of the specimens. The dimensions of the cross-sections measured before the tests were used in the FEM. The ultimate capacities obtained by using FEM indicated a maximum error of 1.3 percent for specimen C7508-CH5-1 with a mesh size of $5\text{ mm} \times 5\text{ mm}$ and $10\text{ mm} \times 10\text{ mm}$. So the mesh size of $10\text{ mm} \times 10\text{ mm}$ was selected to model specimens in order to reduce the analysis time. The ideal elastoplastic model based on the material properties obtained from the coupon tests shown in Table 2 was used in FEM. The end constraint conditions of the test plate were all fixed by constraining the five degrees of freedom of the reference point RP1 at the



FIGURE 8: Buckling modes for specimen C8008-CH3-1. (a) Local buckling. (b) Distortional buckling. (c) Flexure-torsional buckling.



FIGURE 9: Flexural-torsional buckling for specimen C7510-RH6-1.

upper end plate (2 translation degrees of freedom and 3 rotational degrees of freedom, releasing UZ degrees of freedom to control displacement) and the six degrees of freedom of the reference point RP2 at the lower end plate. The measured actual dimensions of the specimens (see in Table 1) were all included in the models. The whole analysis procedure included two phases: Firstly, an eigenvalue buckling analysis was performed to find the most probable elastic buckling mode of the specimen. The measured maximum magnitude of the initial geometric imperfections shown in Table 1 was applied to the first eigenmode to produce the geometric imperfection of FEM. Secondly, nonlinear analysis considering both materials nonlinear and

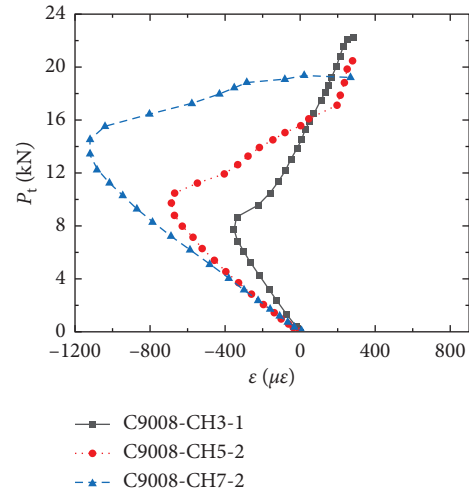


FIGURE 10: Load-strain curve for section C9008 with different circular hole sizes.

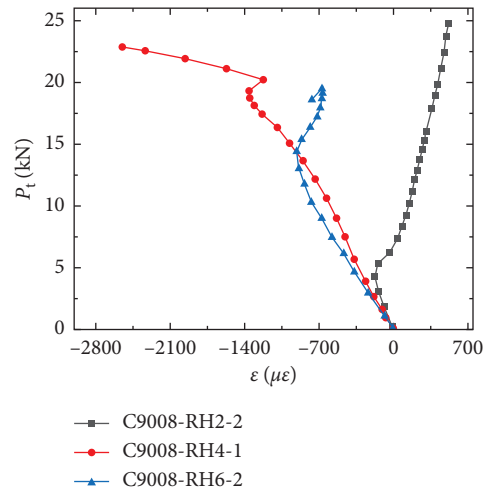


FIGURE 11: Load-strain curve for section C9008 with different rectangular hole sizes.

geometric nonlinear was carried out by using the arc-length method to analyze the failure modes and ultimate load capacity of specimens.

The failure buckling modes and load-carrying capacities of all 42 specimens obtained by FEA are presented in Table 3. The maximum deviation value about the ultimate load capacity between the FEA and test is 10%. The mean value of the test-to-FEA ratio for load capacity is 0.989, with the corresponding coefficient of variation (COV) of 0.039 for all specimens. Specimen C8008-CH7-1 and specimen C7510-RH6-1 are taken as examples to present failure buckling mode comparisons between FEA and test results, as shown in Figures 16 and 17. The comparison of load-displacement curves for specimen C9008-20-CH3-1 between FEA results and the test results is shown in Figure 18. As shown in Figure 18, it should be noted that the load-displacement curves dropped abruptly because of the use of high-strength steel, which leads to the effect of the difference of boundary conditions between test and finite element can be ignored.

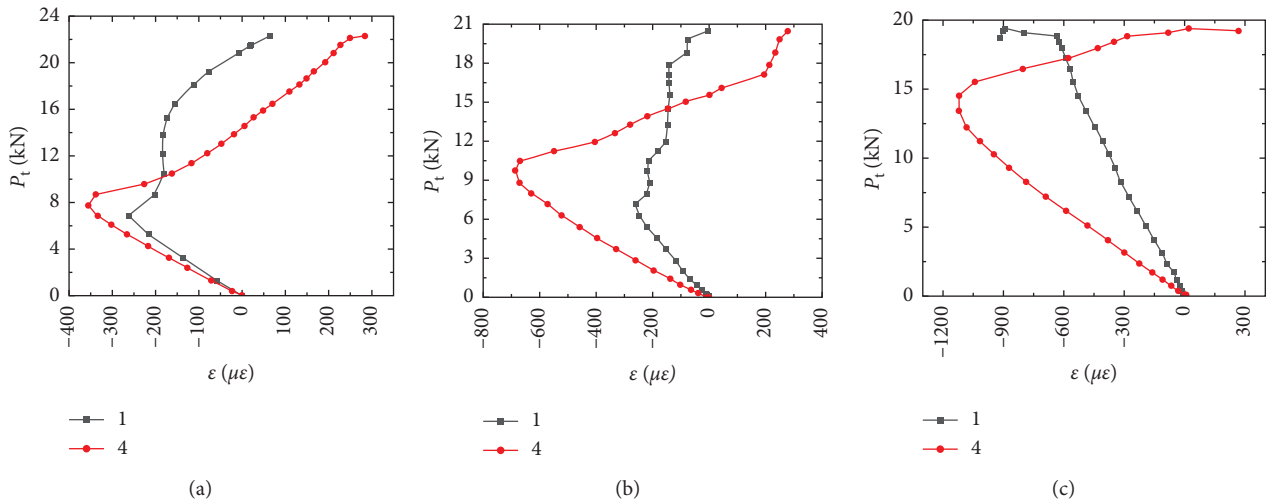


FIGURE 12: Load-strain curves for section C9008 with circular holes for No. 1 and No. 4 strain gauges. (a) Specimen C9008-CH3-1. (b) Specimen C9008-CH5-2. (c) Specimen C9008-CH7-2.

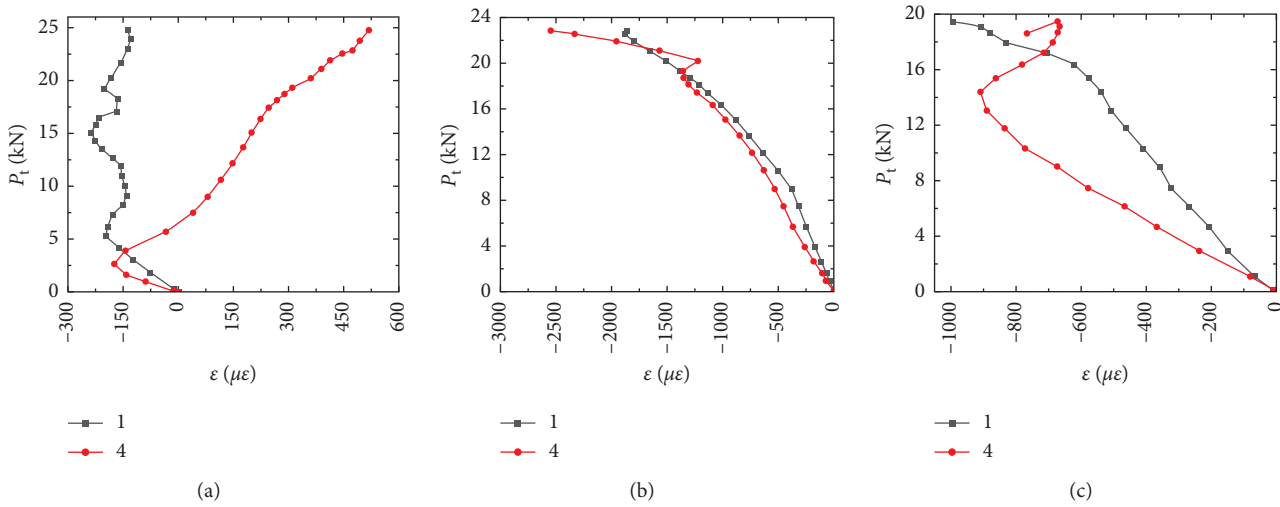


FIGURE 13: Load-strain curve for section C9008 with rectangular holes for No. 1 and No. 4 strain gauges. (a) Specimen C9008-RH2-2. (b) Specimen C9008-RH4-1. (c) Specimen C9008-RH6-2.

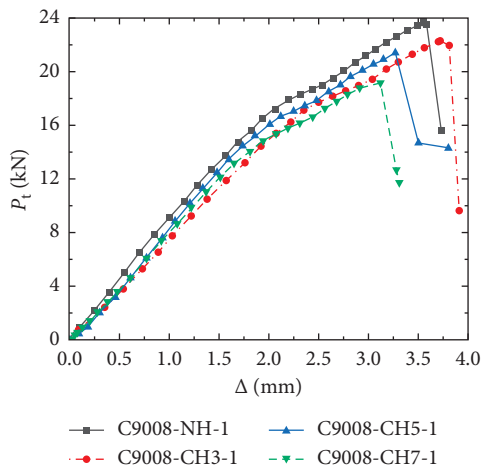


FIGURE 14: Load-displacement curves of section C9008 with circular holes.

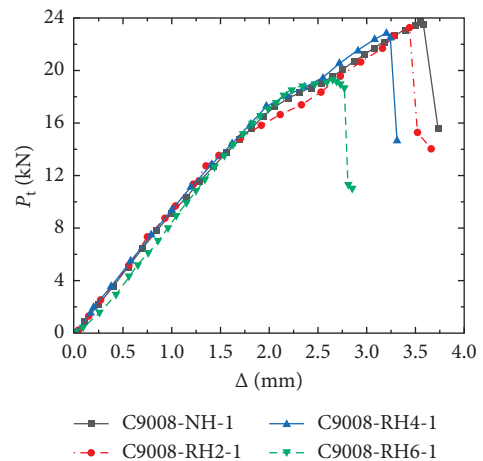


FIGURE 15: Load-displacement curves of section C9008 with rectangular holes.

Although boundary conditions employed in the testing are not perfectly in line with the fix-ended conditions used in the FEA, the above-mentioned comparison indicates that the load-carrying capacities, the failure modes, and load-displacement curves obtained from FEA show good agreement with the test results. Therefore, the FEM developed in this study has been well validated with the tests.

5. Finite Element Parametric Study

FE parametric analyses on 36 CFS lipped channel columns with various cross-section dimensions and sizes of web holes were carried out by using the validated FEM. The web height ranges from 70 to 100 mm and the plate thicknesses are 1.0 and 1.2 mm. The circular hole diameter-to-web depth ratio is 0.3 and 0.7. The rectangular hole height-to-web depth ratio is 0.3 and 0.5. The hole height-to-length ratio is 0.5 for all rectangular holes. The labeling rule for FEA members is the same as the one for test specimens, as shown in Figure 2, except that the last digit in FEA represents the number of holes. The results of ultimate load capacity obtained from FEA (P_a) are listed in Tables 4 and 5 for CFS lipped channel columns with circular and rectangular holes, respectively.

Tables 4 and 5 show that the axial capacities of CFS channels with circular holes and rectangular holes were reduced as the column slenderness increased. For example, the axial capacity was reduced by 69.4% for C8910-RH3 columns when the length of the column increased from 600 mm to 3000 mm. Meanwhile, it can be found that the effect of the hole size on the axial capacity of the CFS lipped channels with holes was significant. For example, when the ratio d/h increased from 0.3 to 0.7, the axial capacity of section C8910-CH-1 decreased by 34.23%.

6. Modified Design Method for Columns with Web Holes

The test results and FEA results indicate that the web holes influence the load capacity of CFS lipped channel axially compressed columns. Therefore, the modified equation (1) is used to predict the design strength of CFS lipped channel columns with web holes under axial compression.

$$N = \varphi_h \cdot A_{eh} \cdot f_y, \quad (1)$$

where φ_h and A_{eh} are the modified global buckling coefficient and effective section area of compression members with web holes, and f_y is the material yield strength. It needs to note that the hole spacings should be more than 2 timing the diameter of the circular hole and 4 timing the height of the rectangular hole.

6.1. *Modified Global Buckling Coefficient of Compression Members with Web Holes.* The global buckling coefficient for CFS axially compressed columns without holes can be determined with the following:

$$\varphi = \frac{P_{cre}}{P_y} = \frac{1}{2} \left\{ 1 + \frac{1}{\bar{\lambda}^2} (1 + \varepsilon_0) - \sqrt{\left[1 + \frac{1}{\bar{\lambda}^2} (1 + \varepsilon_0) \right]^2 - \frac{4}{\bar{\lambda}^2}} \right\}, \quad (2)$$

where $\bar{\lambda} = \lambda/\pi\sqrt{f_y/E}$, λ is the slenderness ratio, $\lambda = L/\sqrt{I/A}$, L is the effective length of the column, I is the moment of inertia of cross section about the axis of buckling, A is the area of gross cross section, ε_0 is the initial eccentricity, P_{cre} and P_y are critical global buckling strength and yield strength, and P_{cre} can be calculated as follows for global flexural buckling:

$$P_{cre} = \frac{\pi^2 EI}{L^2} = \frac{\pi^2 EA}{\lambda^2}. \quad (3)$$

For CFS lipped channel columns with holes, Moen and Schafer [24] proposed the approximate prediction method for critical elastic flexural buckling strength (P_{cre}), which can be dominated by the weighted average method and the prediction equation is as follows:

$$P_{cre,h} = \frac{\pi^2 E}{L^2} \left(\frac{I_g L_g + I_{net} L_{net}}{L} \right) = \frac{\pi^2 EA}{\lambda_h^2}, \quad (4)$$

where I_g , L_g are the moment of inertia of nominal gross cross section about the axis of buckling and segment length without holes, respectively, I_{net} , L_{net} are the moment of inertia of net cross section about the axis of buckling and length of holes, respectively, λ_h is the slenderness ratio considering the effect of holes.

Section $75 \times 30 \times 10 \times 2.5$ is used as an example to verify the accuracy and applicability of equation (4). The comparisons of the critical elastic flexural buckling strength between predicted results with different methods and FEA results are plotted in Figure 19, where P_{cre} , P_{net} , and $P_{cre,h}$ are FEA results, the predicted results with the moment of inertia of net cross section, and the predicted results with equation (4), respectively. It can be observed that the predictions using the net section are too conservative and the predictions with formula (4) are unconservative for members with large web holes. Therefore, equation (4) is modified as equation (5) to give more reliable prediction results for the critical elastic flexural buckling strength of CFS lipped channel columns with web hole based FEA.

$$P_{mcre,h} = \frac{\pi^2 E}{L^2} \left(\frac{I_g L_g + I_{net} L_{net}}{L} \right) \left[1 + 0.08 \left(\frac{H_h}{h} \right) - 0.3 \left(\frac{H_h}{h} \right)^2 \right] \left[1 - \left(\frac{nL_h}{L} \right)^2 \right] = \frac{\pi^2 EI_h}{L^2} = \frac{\pi^2 EA}{\lambda_{mh}^2}, \quad (5)$$

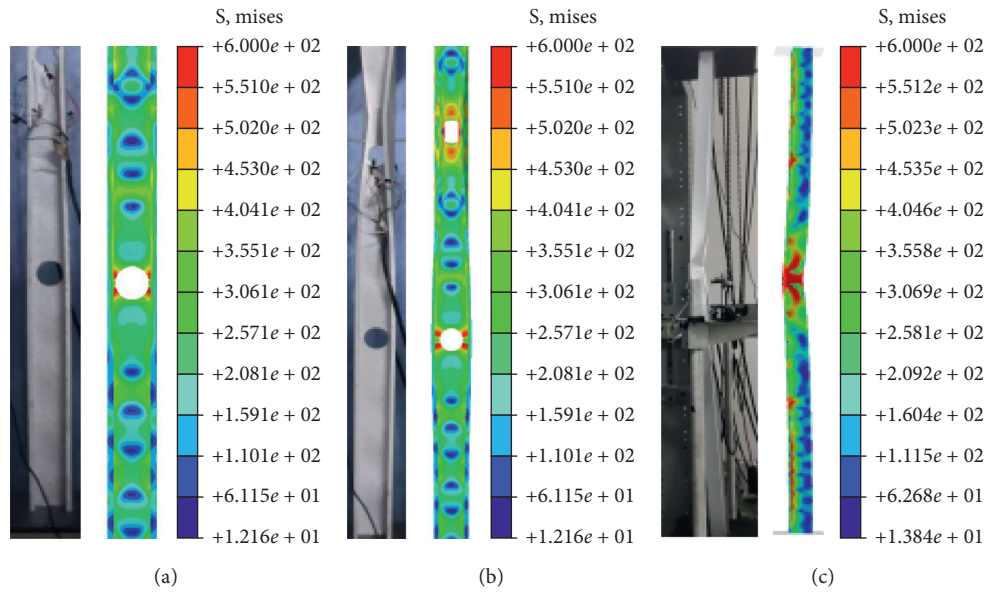


FIGURE 16: Comparison on buckling modes for specimen C8008-CH7-1. (a) Local buckling. (b) Distortional buckling. (c) Flexural buckling.

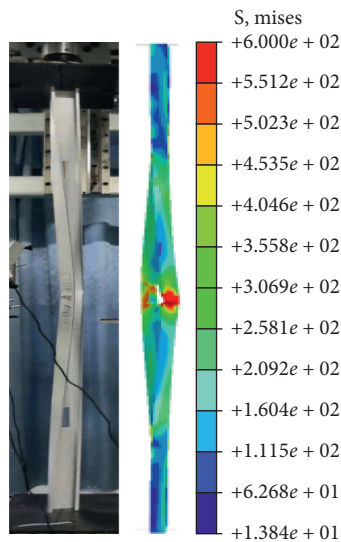


FIGURE 17: Comparison of buckling modes for specimen C7510-RH6-1.

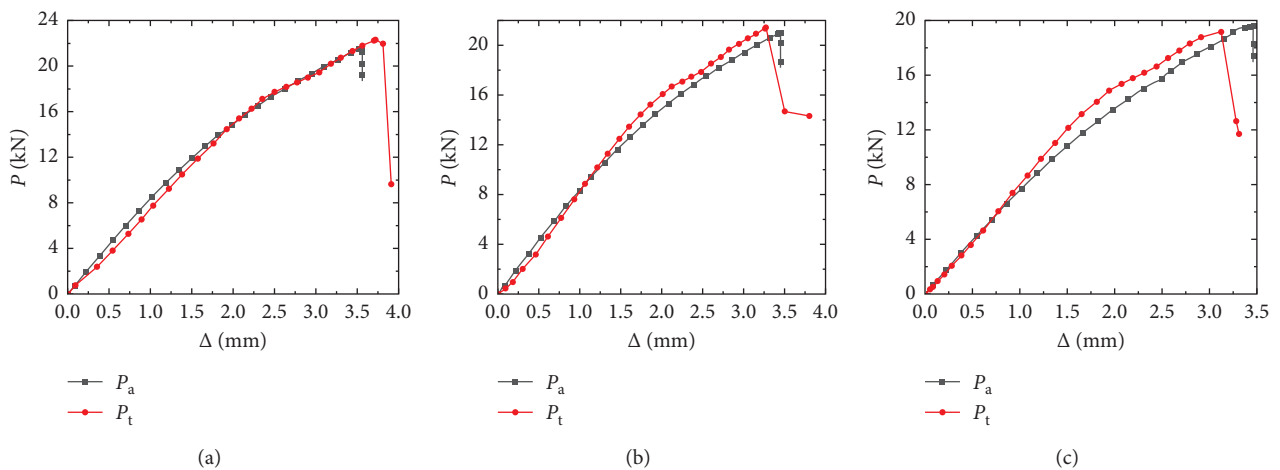


FIGURE 18: Comparison of the load-displacement curve for specimen C9008 between FEA and test. (a) Specimen C9008-CH3-1. (b) Specimen C9008-CH5-1. (c) Specimen C9008-CH7-1.

TABLE 4: Comparison of ultimate strength between the FEA results and the predicted results by using the modified method for columns with circular holes.

Specimen	L (mm)	h (mm)	b (mm)	a (mm)	t (mm)	f_y (MPa)	S (mm)	Hole number	d (mm)	P_a (kN)	P_c (kN)	P_c/P_a
C8910-CH3-6	3000	89	40	13	1	280	500	6	26.7	9.30	9.13	0.98
C8910-CH3-3	1500	89	40	13	1	280	500	3	26.7	21.31	23.27	1.09
C8910-CH3-1	600	89	40	13	1	280		1	26.7	31.87	30.58	0.96
C8910-CH7-6	3000	89	40	13	1	280	500	6	62.3	7.94	7.94	1.00
C8910-CH7-3	1500	89	40	13	1	280	500	3	62.3	17.58	16.17	0.92
C8910-CH7-1	600	89	40	13	1	280		1	62.3	20.96	18.75	0.90
C7012-CH3-6	3000	70	35	11	1.2	350	500	6	21	7.71	7.11	0.92
C7012-CH3-3	1500	70	35	11	1.2	350	500	3	21	27.03	24.35	0.90
C7012-CH3-1	600	70	35	11	1.2	350		1	21	44.00	43.48	0.99
C7012-CH7-6	3000	70	35	11	1.2	350	500	6	49	6.74	6.90	1.02
C7012-CH7-3	1500	70	35	11	1.2	350	500	3	49	20.02	18.07	0.90
C7012-CH7-1	600	70	35	11	1.2	350		1	49	27.36	24.75	0.91
C10010-CH3-6	3000	100	50	12	1	550	500	6	30	13.80	13.37	0.97
C10010-CH3-3	1500	100	50	12	1	550	500	3	30	36.68	34.59	0.94
C10010-CH3-1	600	100	50	12	1	550		1	30	46.40	42.83	0.92
C10010-CH7-6	3000	100	50	12	1	550	500	6	70	12.73	12.97	1.02
C10010-CH7-3	1500	100	50	12	1	550	500	3	70	30.48	28.23	0.93
C10010-CH7-1	600	100	50	12	1	550		1	70	32.85	29.88	0.91
Average												0.954
Standard deviation												0.054
Coefficient of variation												0.057

TABLE 5: Comparison on ultimate strength between the FEA results and predicted results using the modified method for columns with rectangular holes.

Specimen	L (mm)	h (mm)	b (mm)	a (mm)	t (mm)	f_y (MPa)	S (mm)	Hole number	H_h (mm)	L_h (mm)	P_a (kN)	P_c (kN)	P_c/P_a
C8910-RH3-6	3000	89	40	13	1	280	500	6	26.7	53.4	9.20	9.07	0.99
C8910-RH3-3	1500	89	40	13	1	280	500	3	26.7	53.4	20.85	22.95	1.10
C8910-RH3-1	600	89	40	13	1	280		1	26.7	53.4	30.07	30.03	1.00
C8910-RH5-6	3000	89	40	13	1	280	500	6	44.5	89	8.58	8.84	1.03
C8910-RH5-3	1500	89	40	13	1	280	500	3	44.5	89	21.38	19.62	0.92
C8910-RH5-1	600	89	40	13	1	280		1	44.5	89	25.81	23.92	0.93
C7012-RH3-6	3000	70	35	11	1.2	350	500	6	21	42	7.64	7.07	0.93
C7012-RH3-3	1500	70	35	11	1.2	350	500	3	21	42	26.17	24.20	0.92
C7012-RH3-1	600	70	35	11	1.2	350		1	21	42	42.55	42.99	1.01
C7012-RH5-6	3000	70	35	11	1.2	350	500	6	35	70	7.19	6.93	0.96
C7012-RH5-3	1500	70	35	11	1.2	350	500	3	35	70	23.06	21.04	0.91
C7012-RH5-1	600	70	35	11	1.2	350		1	35	70	33.77	31.28	0.93
C10010-RH3-6	3000	100	50	12	1	550	500	6	30	60	13.56	13.30	0.98
C10010-RH3-3	1500	100	50	12	1	550	500	3	30	60	34.16	32.05	0.94
C10010-RH3-1	600	100	50	12	1	550		1	30	60	43.52	42.02	0.97
C10010-RH5-6	3000	100	50	12	1	550	500	6	50	100	13.14	13.02	0.99
C10010-RH5-3	1500	100	50	12	1	550	500	3	50	100	31.40	29.37	0.94
C10010-RH5-1	600	100	50	12	1	550	0	1	50	100	38.96	36.56	0.94
Average												0.965	
Standard deviation												0.049	
Coefficient of variation												0.051	

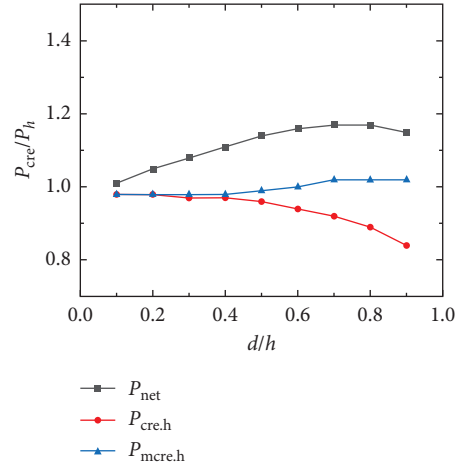


FIGURE 19: Comparison of elastic flexural buckling capacity between FE results and predicted results.

where I_h and λ_{mh} are the modified moments of inertia of gross cross section about the axis of buckling and slenderness ratio considering the effect of holes.

The comparison of critical global buckling strength between FEA results and predicted results ($P_{mcre,h}$) by using equation (5) shown in Figure 19 indicates that formula (5) is accurate.

Based on formulas (3) and (5), the following equation can be obtained:

$$\frac{\lambda_{mh}}{\lambda} = \sqrt{\frac{P_{cre}}{P_{mcre,h}}} = \sqrt{\frac{I}{I_h}}, \quad (6)$$

where $I_h = (I_g L_g + I_{net} L_{net}/L) [1 + 0.08(H_h/h) - 0.3(H_h/h)^2][1 - (nL_h/L)^2]$, then the modified global buckling coefficient can be determined using the following:

$$I_{th} = \left(\frac{I_{tg} L_g + I_{tnet} L_{net}}{L} \right) \left[1 + 0.08 \left(\frac{H_h}{h} \right) - 0.3 \left(\frac{H_h}{h} \right)^2 \right] \left[1 - \left(\frac{nL_h}{L} \right)^2 \right], \quad (8)$$

where I_{tg} and I_{tmet} are Saint-Venant torsion constants of gross cross section and net cross section.

For CFS lipped channel axially compressed members with a circular hole, the diameter d can be used to replace H_h and L_h in equations (5) and (8).

6.2. Modified Effective Area Equation for Compression Members with Web Holes. The effective area of CFS axially compressed stud columns with holes can be determined by using the modified effective width method in [34]. However, it needs to note that the effect of web holes on the effective area will decrease with the increase of the length of columns. Therefore, the effective areas of CFS columns with different lengths can be predicted by using equation (9), considering the effect of dimensions of holes and the length of columns based on FEA results.

$$\begin{aligned} \varphi_h &= \frac{P_{mcre,h}}{P_y} \\ &= \frac{1}{2} \left\{ 1 + \frac{1}{\bar{\lambda}_{mh}^2} (1 + \varepsilon_0) - \sqrt{\left[1 + \frac{1}{\bar{\lambda}_{mh}^2} (1 + \varepsilon_0) \right]^2 - \frac{4}{\bar{\lambda}_{mh}^2}} \right\}, \end{aligned} \quad (7)$$

where $\bar{\lambda}_{mh} = \lambda_{mh}/\pi\sqrt{f_y/E}$, λ_{mh} is the modified slenderness ratio considering the effect of holes which can be calculated by using equation (6).

For the global flexural-torsional buckling coefficient of CFS axially compressed columns with holes, equation (7) can also be used. Saint-Venant torsion constant can be calculated using equation (8) and the warping constant can be predicted assuming cross-section thickness is zero at the hole as reported in [34].

$$A_{eh} = \begin{cases} A_{e1}, & \bar{\lambda} \leq \frac{0.561A}{A_{net}}, \\ \left(1 + \frac{\bar{\lambda} - \bar{\lambda}_1}{\bar{\lambda}_2 - \bar{\lambda}_1} \cdot \frac{A_{e2} - A_{e1}}{A_{e1}} \right) A_{e1}, & \frac{0.561A}{A_{net}} < \bar{\lambda} < \frac{1.5A}{A_{net}}, \\ A_{e2}, & \bar{\lambda} \geq \frac{1.5A}{A_{net}}, \end{cases} \quad (9)$$

where A_{e1} , A_{e2} are the effective area considering the effect of holes using the modified effective width method in [16] and the effective area without considering the effect of holes. A_{net} is the net sectional area, $\bar{\lambda}$ is the normalized slenderness ratio of columns, and $\bar{\lambda}_1 = 0.561A/A_{net}$, $\bar{\lambda}_2 = 1.5A/A_{net}$.

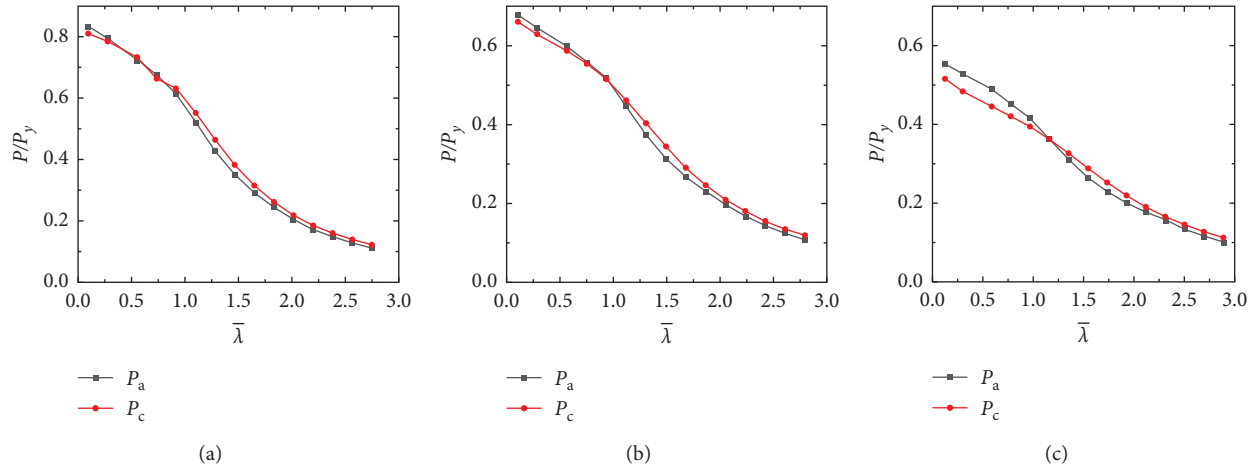


FIGURE 20: Comparison of the ultimate capacity of columns with circular holes between FEA results and predicted results using the modified method. (a) $d/h = 0.3$. (b) $d/h = 0.5$. (c) $d/h = 0.7$.

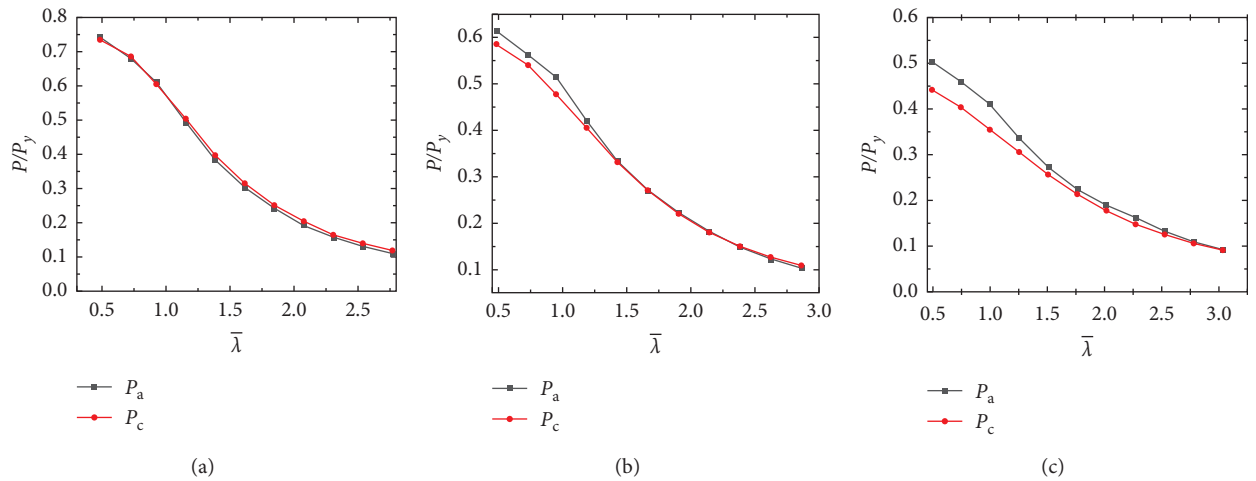


FIGURE 21: Comparison of ultimate capacity of columns with rectangular holes between FEA results and predicted results using the modified method ($H_h:L_h = 1:2$). (a) $H_h/h = 0.3$. (b) $H_h/h = 0.5$. (c) $H_h/h = 0.7$.

6.3. Comparison of Design Capacity with Test and FEA Data.

The load capacities determined by the modified design formula (1) were compared with the ultimate capacities obtained from tests and FE analyses, as listed in Tables 3–5. The mean value of the test-to-prediction ultimate strength ratio (P_t/P_c) is 1.008 with the corresponding standard deviation of 0.04, as shown in Table 3. The mean values of prediction-to-FEA ultimate strength ratios (P_c/P_a) are 0.954 and 0.965 with the corresponding standard deviation of 0.054 and 0.049 for columns with circular and rectangular holes as listed in Tables 4 and 5, respectively.

Figures 20 and 21 show that the modified load capacity curves for section $75 \times 30 \times 10 \times 2.5$ with the size of circular holes $d/h = 0.3, 0.5,$ and 0.7 and rectangular holes $H_h/h = 0.3, 0.5,$ and 0.7 give good agreement with the FEA results for CFS lipped channel columns with web holes, respectively, where P_a and P_c are FEA and predicted load capacities, P_y is the yield strength.

The comparison results shown in Tables 3–5 and Figures 20 and 21 indicate that the predicted results by using a

modified formula based on modified global buckling coefficient and modified effective area are extremely accurate.

7. Conclusions

This paper presents a total of 42 experimental results on the axial strength of CFS lipped channels with circular holes, rectangular holes, and without holes. Based on the experimental and numerical results presented in this paper, the following conclusions can be drawn:

- (1) It was found that all specimens with a large width-to-thickness ratio exhibited the interaction of local buckling, distortional buckling, and global buckling, while specimens with a small width-to-thickness ratio displayed global buckling. The width to thickness of the plate adjacent to the hole decreased with the increase of the hole size, so buckling stress and the buckling load gradually increased. The axial strength of the CFS lipped channel with holes

gradually decreased with the increase of the hole size. The axial strength decreased maximum by 20.48% and 22.98% for the same sections with circular holes and rectangular holes, compared to the member without web holes.

- (2) A nonlinear FE model was developed, showing a good agreement with the test results both in terms of ultimate strength and buckling mode. Using the validated FEM, a parametric study comprising 36 models was conducted to investigate the effects of column slenderness and size of the hole on the axial strength of such channels. The results obtained from the parametric study show that the axial capacity of CFS lipped channels with holes was greatly decreased due to the presence of holes and the effects of the hole size on the axial capacity of such sections were significant. The axial capacities of CFS lipped channels with holes were decreased with the increase of the column slenderness. The proven FEM was used to develop the global buckling coefficient equation and effective area formula of the CFS lipped channel section under axial compression considering the effect of holes.
- (3) An improved design equations based on the developed global buckling coefficient equation and effective area formula were developed in this paper. The results obtained from numerical analysis and tests were compared against the design strengths determined from the developed design method for CFS lipped channels with holes. It was found that the developed design method can closely predict the axial strength of CFS lipped channel columns with holes, being only 4.6% maximum on average to experimental and numerical results.

Data Availability

The data used to support the findings of this study are available upon request to the author.

Conflicts of Interest

The author declares that there are no conflicts of interest regarding the publication of this paper.

Acknowledgments

This research was funded by the National Natural Science Foundation Projects of China (Grant no. 51868049), Natural Science Foundation Projects of Jiangxi Province in China (Grant no. 20181BAB206040), and Department of Education Science and Technology Projects of Jiangxi Province in China (Grant nos. GJJ180932 and GJJ170983).

References

- [1] R. A. O. Colberg, *The Load Carrying Capacity of Perforated Cold-Formed Steel Columns*, Thesis, Cornell University, NY, USA, 1981.
- [2] N. A. Rahman, *Cold-formed Steel Compression Members with Perforations*, Thesis, McMaster University, Hamilton, Canada, 1997.
- [3] K. S. Sivakumaran, "Load capacity of uniformly compressed cold-formed steel section with punched web," *Canadian Journal of Civil Engineering*, vol. 14, no. 4, pp. 550–558, 1987.
- [4] B. He and G. Zhao, "Analysis on buckling behavior of cold-formed lipped channel with perforated web," *Journal of Xi'an Institute Metallica & Construction Engineering*, vol. 21, no. 1, pp. 1–9, 1989, In Chinese.
- [5] Y. Yao, Z. Wu, B. Cheng et al., "Experimental investigation into axial compressive behavior of cold-formed thin-walled steel columns with lipped channel and openings," *Journal of South China University of Technology*, vol. 39, no. 9, pp. 61–67, 2011, In Chinese.
- [6] C. D. Moen and B. W. Schafer, "Direct strength method for design of cold-formed steel columns with holes," *Journal of Structural Engineering, ASCE*, vol. 137, no. 5, pp. 559–570, 2016.
- [7] C. D. Moen and B. W. Schafer, "Experiments on cold-formed steel columns with holes," *Thin-Walled Structures*, vol. 46, no. 10, pp. 1164–1182, 2008.
- [8] M. P. Kulatunga and M. Macdonald, "Investigation of cold-formed steel structural members with perforations of different arrangements subjected to compression loading," *Thin-Walled Structures*, vol. 67, pp. 78–87, 2013.
- [9] M. P. Kulatunga, M. Macdonald, J. Rhodes, and D. K. Harrison, "Load capacity of cold-formed column members of lipped channel cross-section with perforations subjected to compression loading - part I: FE simulation and test results," *Thin-Walled Structures*, vol. 80, pp. 1–12, 2014.
- [10] C. H. Pham, "Shear buckling of plates and thin-walled channel sections with holes," *Journal of Constructional Steel Research*, vol. 128, pp. 800–811, 2017.
- [11] S. H. Pham, C. H. Pham, and G. J. Hancock, "Direct strength method of design for channel sections in shear with square and circular web holes," *Journal of Structure Engineering*, vol. 143, no. 6, Article ID 04017017, 2017.
- [12] P. Keerthan and M. Mahendran, "Improved shear design rules for lipped channel beams with web openings," *Journal of Constructional Steel Research*, vol. 97, pp. 127–142, 2014.
- [13] P. Keerthan and M. Mahendran, "Experimental studies of the shear behaviour and strength of lipped channel beams with web openings," *Thin-Walled Structures*, vol. 73, pp. 131–144, 2013.
- [14] C. D. Moen, A. Schudlic, and A. V. Heyden, "Experiments on cold-formed steel C-section joists with unstiffened web holes," *Journal of Structure Engineering*, vol. 139, no. 5, pp. 695–704, 2013.
- [15] J. Zhao, K. Sun, C. Yu et al., "Tests and direct strength design on cold-formed steel channel beams with web holes," *Engineering Structures*, vol. 184, pp. 434–446, 2019.
- [16] J. Zhao, P. Gao, J. Wang et al., "Local buckling behavior and direct strength method of cold-formed steel channel beams with web rectangular openings and complex edge stiffeners," *Journal of Building Structures*, vol. 41, no. 6, pp. 195–204, 2020, (In Chinese).
- [17] B. Chen, K. Roy, A. Uzzaman et al., "Effects of edge-stiffened web openings on the behaviour of cold-formed steel channel sections under compression," *Thin-Walled Structures*, vol. 144, Article ID 106307, 2019.
- [18] B. Chen, K. Roy, A. Uzzaman et al., "Parametric study and simplified design equations for cold-formed steel channels with edge-stiffened holes under axial compression," *Journal of*

- Constructional Steel Research*, vol. 144, Article ID 106161, 2020.
- [19] B. Chen, K. Roy, A. Uzzaman et al., "Axial strength of back-to-back cold-formed steel channels with edge-stiffened holes, unstiffened holes and plain webs," *Journal of Constructional Steel Research*, vol. 174, Article ID 106313, 2020.
- [20] A. Uzzaman, J. B. P. Lim, D. Nash et al., "Web crippling behaviour of cold-formed steel channel sections with edge-stiffened and unstiffened circular holes under interior-two-flange loading condition," *Thin-Walled Structures*, vol. 154, Article ID 106813, 2020.
- [21] A. Uzzaman, J. B. P. Lim, D. Nash et al., "Cold-formed steel channel sections under end-two-flange loading condition: design for edge-stiffened holes, unstiffened holes and plain webs," *Thin-Walled Structures*, vol. 147, Article ID 106532, 2020.
- [22] M. L. Dung, P. T. Chung, J. L. Liu et al., "The compressive strength of slender C-shaped cold-formed steel members with web openings," *International Journal of Steel Structure*, vol. 9, no. 3, pp. 231–240, 2009.
- [23] T. Kawai and H. Ohtsubo, "A Method of Solution for the Complicated Buckling Problems of Elastic Plates with Combined Use of Rayleigh–Ritz's Procedure in the Finite Element Method," in *Proceedings of the Second Conference on Matrix Methods in Structural Mechanics*, pp. 967–994, OH, USA, October 1968.
- [24] C. D. Moen and B. W. Schafer, "Elastic buckling of cold-formed steel columns and beams with holes," *Engineering Structures*, vol. 31, no. 12, pp. 2812–2824, 2009.
- [25] X. Yao, Y. Guo, Y. Liu et al., "Analysis on distortional buckling of cold-formed thin-walled steel lipped channel steel members with web openings under axial compression," *Industrial Construction*, vol. 50, no. 1, pp. 170–177, 2020, In Chinese.
- [26] Y. Liu, X. Yao, and J. Su, "Analysis of elastic buckling performance of open-hole thin plates under axial compression," *Journal of Ningxia University (Natural Science Edition)*, vol. 40, no. 1, pp. 45–51, 2019, In Chinese.
- [27] American Iron and Steel Institute, *North American Specification for the Design of Cold-formed Steel Structural Members*, Canadian Standards Association, Mississauga, Canada, 2016.
- [28] Joint Technical Committee BD-082, Australia/New Zealand Standard, *Cold-Formed Steel Structures*, SAI Global, Sydney, Australia, 2018.
- [29] Ministry of Housing and Urban-Rural Development of the People's Republic of China, Chinese National Standard, *Technical Code for Cold-Formed Thin-Walled Steel Structures*, Chinese Planning Press, Beijing, China, 2002, In Chinese.
- [30] General Administration of Quality Supervision, Inspection and Quarantine of the People's Republic of China, *Test Method for Tensile Test Room Temperature of Metallic Materials*, China Standard Press, Beijing, China, 2011, In Chinese.
- [31] Y. Guo and X. Yao, "Experimental study and effective width method for cold-formed steel lipped channel stud columns with holes," *Advances in Civil Engineering*, vol. 2021, Article ID 9949199, 16 pages, 2021.
- [32] X. Yao, *Buckling Behavior and Effective Width Method of Perforated Cold-Formed Steel Slender Columns under Axial Compression*, Research of Report, Nanchang Institute of Technology, Nanchang, China, 2020, In Chinese.
- [33] ABAQUS, *ABAQUS/Standard User's Manual Volumes I-III and ABAQUS CAE Manual*, Dassault Systemes Simulia Corporation, RI, USA, 2014.
- [34] X. Song, *Experiment and Design Method of Cold-Formed Thin-Walled Steel Stud with Web Hole*, Nanchang Institute of Technology, Nanchang, China, 2020, In Chinese.